Journal of Materials Chemistry A

PAPER

View Article Online
View Journal | View Issue

Cite this: J. Mater. Chem. A, 2019, 7, 27514

Heterostructured intermetallic CuSn catalysts: high performance towards the electrochemical reduction of CO_2 to formate†

Jigang Wang,‡[a] Jiasui Zou,‡[a] Xiao Hu,[a] Shunlian Ning,[a] Xiujun Wang,[b] Xiongwu Kang *[a] and Shaowei Chen *[c]

Received 9th October 2019
Accepted 21st November 2019

DOI: 10.1039/c9ta11140a

rsc.li/materials-a

Electroreduction of carbon dioxide (CO_2RR) into fuels and chemicals is an appealing approach to tackle CO_2 emission challenges. To this end, it is critical to develop highly efficient and selective electrocatalysts for the CO_2RR. Herein, we report a simple strategy for the preparation of heterostructured intermetallic CuSn electrocatalysts (Cu_3Sn/Cu_6Sn_5) supported on porous copper foam through an electrodeposition–calcination process. The obtained CuSn intermetallic catalysts demonstrate a faradaic efficiency of 82% and a current density of 18.9 mA cm^{-2} at −1.0 V *vs.* the reversible hydrogen electrode for formate production in 0.1 M $NaHCO_3$ electrolyte for as long as 42 h. By using a gas diffusion electrode and 1 M KOH electrolyte, the current density of this catalyst for formic acid production can reach values as high as 148 mA cm^{-2}. Density functional theory calculations show that the moderate Gibbs free energy of hydrogen adsorption on the heterostructured Cu_3Sn/Cu_6Sn_5 catalysts not only suppresses hydrogen evolution, but also favors the production of formic acid. This study demonstrates a straightforward approach to the preparation of high-performance electrocatalysts towards the selective electroreduction of CO_2 to formate.

Introduction

Electrochemical reduction of carbon dioxide into value-added chemicals and fuels (CO, CH_4, C_2H_4, CH_3OH, HCOOH, *etc.*) by using intermittent renewable and clean energy has been attracting extensive attention due to its fundamental and technological importance.[1–3] Thus, extensive efforts have been devoted to the rational design, synthesis and surface engineering of highly selective and active electrocatalysts, where understanding of the reaction mechanism of electrochemical reduction of CO_2 (CO_2RR) has remained a critical challenge. For instance, Shao and coworkers reported the synthesis of core–shell structured and grain-boundary rich Pd–Au nanowires and explored in detail the structural and compositional effects on the electrochemical performance of the CO_2RR.[4] The best Pd–Au catalyst showed a faradaic efficiency (FE) of 94.3% for CO production at −0.6 V *vs.* the reversible hydrogen electrode (RHE). Besides, the authors observed the reaction intermediates of the CO_2RR, such as adsorbed CO in linear and bridging modes, and $*COO^-$, *COOH, *OCHO, *etc.* by using an attenuated total reflection configuration and isotopic labeling on various electrocatalysts.[5,6] Zhang and coworkers reported the CO_2RR on PdS nanocrystal catalysts and monitored the structural evolution of the catalysts by *in situ* synchrotron radiation X-ray diffraction.[7]

Tin and copper based nanomaterials have also been explored as excellent electrocatalysts towards the CO_2RR.[8–16] For example, Cu_4Zn has been found to achieve an FE of 29.1% and a current density of −8.2 mA cm^{-2} for ethanol production at −1.05 V *vs.* RHE.[17] Copper oxide dendrites with surface oxygen vacancies display a FE of 63% towards ethylene production, as reported by Zheng and coworkers.[18] Sarfraz prepared a CuSn alloy and observed an FE of more than 90% for CO production and a current density of −1.0 mA cm^{-2} at −0.6 V *vs.* RHE, much higher than that of oxide-derived copper.[19] PdSn alloys have also shown a nearly perfect FE toward formic acid formation at a very low overpotential of −0.26 V.[20]

In these studies, surface and interface engineering of metal catalysts has been demonstrated as an effective strategy to improve their electrochemical performance.[21–23] For instance, Wang *et al.* prepared 3D flower-like CoP_3/Ni_2P heterostructures by phosphating CoNi-layered double hydroxide (LDH) and observed an improved HER performance. They confirmed that a significant decrease of charge density at the CoP_3/Ni_2P (Co) sites promoted the desorption of produced hydrogen and

[a]New Energy Research Institute, School of Environment and Energy, South China University of Technology, Higher Education Mega Center, 382 East Waihuan Road, Guangzhou 510006, China. E-mail: esxkang@scut.edu.cn

[b]School of Chemistry and Chemical Engineering, South China University of Technology, Guangzhou 510640, China

[c]Department of Chemistry and Biochemistry, University of California, 1156 High Street, Santa Cruz, California 95064, USA. E-mail: shaowei@ucsc.edu

† Electronic supplementary information (ESI) available. See DOI: 10.1039/c9ta11140a

‡ These authors contributed equally to the work.

minimized catalyst poisoning.[24] Zhu *et al.* demonstrated the significance of interfacial engineering of the Co–Ni_3N heterojunction for the HER.[25] However, studies have remained scarce thus far for the far more complicated CO_2RR. Recently, Sen *et al.*[26] found that in the CO_2RR, copper nanofoam exhibited marked differences from smooth copper electrodes in terms of the distribution and FE of the reduction products. Copper foam can also be an excellent catalyst support due to its large surface area, well-defined pore size, and high conductivity.[27] Meanwhile, in view of the high overpotential for the hydrogen evolution reaction, Sn electrodes are also suitable for selective CO_2 reduction with the advantages of relatively high catalytic activity, low cost and low toxicity.[28–31]

In this work, intermetallic CuSn catalysts were prepared by electrochemical deposition of Sn on Cu foam, where thermal annealing led to the formation of heterostructured Cu_6Sn_5/Cu_3Sn (Fig. 1a). The obtained samples showed excellent catalytic activity towards the CO_2RR to produce formate, with a high FE (82%) and a current density of 18.9 mA cm^{-2} in a CO_2-saturated $NaHCO_3$ (0.1 mol L^{-1}) electrolyte solution at −1.0 V *vs.* RHE. Density functional theory (DFT) calculations were carried out to probe the adsorption energy of CO_2RR intermediates and the Gibbs free energy of hydrogen on the various metal surfaces, which advanced our understanding of the catalytic mechanism.

Experimental

Chemicals

Stannous chloride dihydrate ($SnCl_2 \cdot 2H_2O$), potassium hydroxide (KOH) and sodium bicarbonate ($NaHCO_3$) of analytical grade were purchased from Energy Chemicals (Shanghai, China). CO_2 (purity 99.995%), Ar (purity 99.99%) and H_2 (purity 99.999%) were obtained from Guangzhou Messer Gases (Guangzhou, China). All chemicals were used as received. Deionized water was supplied by a Barnstead Nanopure Water System (18.3 MΩ cm).

Sample preparation

Heterostructured intermetallic CuSn catalysts supported on Cu foam were prepared by a two-step procedure. First, Sn nanoparticles were grown on Cu foam by an electrodeposition process. In detail, a piece of Cu foam (10 mm × 12 mm × 1.6 mm, 780 g m^{-2}, Suzhou Taili Materials, China) was pretreated in a 5 M HCl aqueous solution for 30 min to remove any potential copper oxide species on the surface, and then rinsed with deionized water. Sn was then deposited onto the treated Cu foam in a three-electrode cell, with Cu foam as the working electrode, Pt wire as the counter electrode and a Ag/AgCl electrode as the reference electrode, in a 2 M KOH aqueous solution containing 0.05 M $SnCl_2$. A constant current of 5 mA cm^{-2} was applied for varied periods (1000, 2000, and 3000 s) at ambient temperature. A total charge of 5C, 10C or 15C was used for Sn reduction and deposition. The obtained samples, denoted as Cu@Sn5, Cu@Sn10 and Cu@Sn15, respectively, were rinsed with ethanol and dried in N_2. Thermal annealing of the samples at 300 °C for 3 h in a nitrogen atmosphere resulted in the formation of heterostructured CuSn intermetallics, which were denoted as CuSn–5C, CuSn–10C and CuSn–15C, respectively.

Pure-phase Cu_6Sn_5 and Cu_3Sn intermetallic compounds were synthesized by following a reported procedure.[32] In detail, $SnCl_2 \cdot H_2O$ (15.8 mmol) was added into a NaOH (6 M) aqueous solution (30 mL) under magnetic stirring for a few minutes, into which $CuCl_2 \cdot 2H_2O$ (4 mmol) was then added. The obtained solution was transferred to a 100 mL Teflon-lined stainless-steel autoclave and heated at 120 °C for 6 h. After cooling down to room temperature naturally, the precipitates were collected by centrifugation at a speed of 8000 rpm for 3 min and washed four times with ethanol to obtain the final product of Cu_6Sn_5. Cu_3Sn was prepared by following the same protocol except that $CuCl_2 \cdot 2H_2O$ (8 mmol) was used and the reaction temperature was set at 220 °C.

DFT computations

Plane-wave density functional theory (DFT) calculations were performed using the CASTEP code of the Materials Studio package of Accelrys Inc.[10] Generalized gradient approximation (GGA) in the form of Perdew–Burke–Ernzerhof (PBE) functional[9] was employed for the DFT exchange–correlation energy and ultrasoft pseudo-potentials were used for the core electrons. The calculations were conducted on a 4-layer metal slab of Cu_3Sn (111) and Cu_6Sn_5 (111), respectively, using a 2 × 2 periodic cell. The periodic region of Cu_3Sn was ($x = 5.51$ Å, $y = 38.1$ Å, $z = 4.319$ Å) and for Cu_6Sn_5 it was ($x = 11.033$ Å, $y = 7.294$ Å, $z = 9.83$ Å) with an optimized vacuum space of 15 Å. The self-consistent field (SCF) tolerance, the maximum displacement and the energy cut-off were set to 1×10^{-6} eV, 0.001 Å and 400 eV, respectively. For each reaction step, the convergence criteria of the optimal geometry and the geometries for all the states were relaxed until all the forces on the free atoms were 1.0×10^{-5} eV per atom and 0.03 eV $Å^{-1}$. The sampling of the Brillouin zone was performed with a 3 × 3 × 1 Monkhorst–Pack *k*-point mesh. In all metal slabs, the atoms in the two bottom layers were fixed and those in the upper layers were set free in the calculations.

The binding energies of the adsorbates on the metal surfaces ($BE_{adsorbate}$) were calculated using the relationship $BE_{adsorbate} = E_{adsorbate+surface} - (E_{adsorbate} + E_{surface})$, where $E_{adsorbate+surface}$ represents the total energy of the adsorbate interacting with the metal slab, $E_{adsorbate}$ is the energy of the adsorbate in the gas phase, and $E_{surface}$ is the energy of the bare metal surface. The Gibbs free energy (ΔG) of an elementary reaction is defined as $\Delta G = \Delta E_{H^*} + \Delta E_{ZPE} - T\Delta S$, where ΔE_{H^*} is calculated using the relationship $\Delta E_{H^*} = E_{surface+H^*} - (E_{surface} + E_H)$, where $E_{surface+H^*}$ and $E_{surface}$ denote the energy of substrates with an adsorbed H atom and the energy of bare substrates, E_H denotes half of the energy of H_2, ΔE_{ZPE} is the difference in zero-point energy between the final and initial states, and $T\Delta S$ is the entropy change of the elementary reaction.

Results and discussion

The surface morphologies of the Cu foam and CuSn-coated catalysts before and after thermal annealing were first studied

and compared by SEM measurements, as shown in Fig. 1 and S1.† It can be clearly seen that the originally smooth Cu foam surfaces (panels b and e) were covered with a number of small spherical nanoparticles about 50 nm in diameter after electrochemical deposition of Sn (panels c and f), and after thermal annealing at 300 °C the particles were found to exhibit sharp edges and corners (panels d and g), most likely due to the restructuring and formation of CuSn. Upon changing the amount of Sn on the Cu foam, the number of metal nanoparticles increased from CuSn@5 to CuSn@15 (Fig. S1†). Fig. 1h and i show the HRTEM images of Cu–Sn intermetallics scratched from the Cu foam substrate, from which lattice fringe spacings of 0.296 and 0.208 nm were clearly observed, corresponding to the (2 2 −1) facet of Cu_6Sn_5 and (2 1 2 0) facet of Cu_3Sn, respectively (Fig. 1i and S2†). The grain boundaries between the two phases can also be clearly observed, as

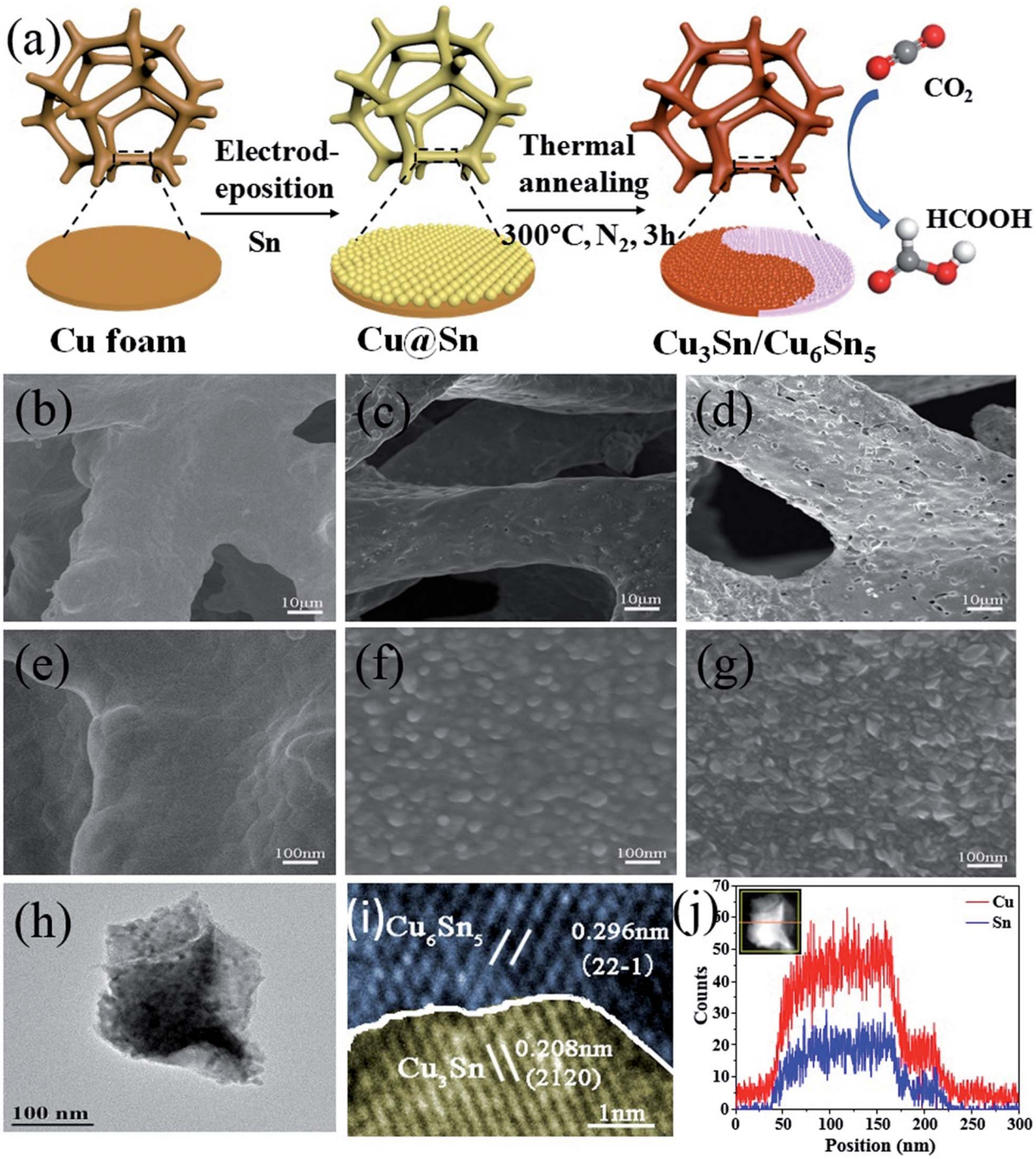

Fig. 1 (a) Schematic illustration of the preparation of heterostructured Cu_3Sn/Cu_6Sn_5 on Cu foam. SEM images of (b and e) Cu foam, (c and f) Cu@Sn10 and (d and g) CuSn–10C. (h and i) TEM and HRTEM images and (j) line-scanning analysis results of CuSn–10C.

highlighted by the two different colors. Line scanning analysis (Fig. 1j) and EDX (Fig. S3†) results show that Sn and Cu were distributed uniformly throughout the particle, suggesting the formation of CuSn intermetallics.

The intermetallic CuSn structures were further characterized by XRD measurements, as shown in Fig. 2 and S4.† All samples exhibit three diffraction peaks at $2\theta = 43.3°$, 50.4° and 74.1°, due to the (111), (200) and (220) planes of face centered cubic (fcc) Cu (PDF 04-0836), respectively. After the electrodeposition of Sn, four characteristic peaks emerged at 30.6°, 32.0°, 44.9° and 62.5°, which can be indexed to the (200), (101), (211) and (112) facets of hexagonal Sn (PDF 04-0673), respectively. Upon annealing, the Sn diffraction patterns disappeared, and a new peak emerged at 30.1°, due to the (2 2 −1) facet of Cu_6Sn_5 (PDF 45-1488), along with three more at 37.7°, 41.7° and 57.5° that can be assigned to the (0160), (002) and (0162) facets of Cu_3Sn (PDF 01-1240). This suggests the successful formation of intermetallic heterostructures after thermal treatment. In addition, based on the XRD patterns, the mass ratio of Cu_6Sn_5 to Cu_3Sn is estimated to be 0.36 : 1 for CuSn–5C, 1.05 : 1 for CuSn–10C, and 0.41 : 1 for CuSn–15C (Table 1). XPS measurements (Fig. S5†) show only Cu and Sn in the samples, indicating high purity of the materials.

The electrochemical activity of the CuSn intermetallics towards the CO_2RR was then evaluated by linear sweep voltammetry (LSV), as shown in Fig. 3a and S6.† It can be seen that the current density in CO_2-saturated $NaHCO_3$ is significantly enhanced, as compared to that under N_2 saturation, suggesting the apparent electrocatalytic activity of the CuSn intermetallics towards the CO_2RR. The product selectivity was further investigated by electrolysis in CO_2-saturated electrolyte for 2 h with the applied potentials varied from −0.8 to −1.2 V (*vs.* RHE). As shown in Fig. 3b, Cu foam mainly produced H_2 at potentials from −0.8 to −1 V, but trace amounts of other carbon products could also be detected (Fig. S7†) and the maximum FE towards HCOOH at −1.2 V was only 28%; yet, upon deposition of Sn, the CO_2RR FE of formate production increased to about 40%, 52% and 60% for Cu@Sn5, Cu@Sn10 and Cu@Sn15 at −1.0 V, respectively, and was further enhanced to 62.5%, 82% and 58.3% for CuSn–5C, CuSn–10C and CuSn–15C. This suggests that thermal annealing and the formation of heterostructured

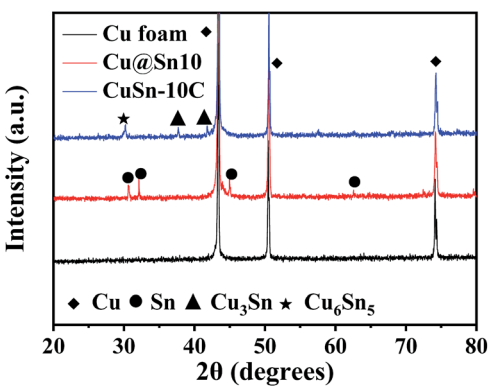

Fig. 2 XRD patterns of Cu foam, Cu@Sn10 and CuSn–10C.

Table 1 Composition proportions in the heterostructured intermetallics

	CuSn–5C	CuSn–10C	CuSn–15C
Cu	47.9%	46%	39.4%
Cu_6Sn_5	38.3%	26.4%	43.1%
Cu_3Sn	13.8%	27.6%	17.5%
Cu_3Sn/Cu_6Sn_5	0.36 : 1	1.05 : 1	0.41 : 1

CuSn intermetallics (Fig. S8a–c†) play a critical role in CO_2RR activity and selective production of formate. It should be noted that only a minimum amount of CO was produced on the CuSn before and after thermal annealing at all applied potentials, and the main competing reaction to formate production was hydrogen evolution.

The total current density and partial geometric current density for HCOOH production at varied applied potentials on CuSn–5C, CuSn–10C and CuSn–15C were then quantified and compared, as shown in Fig. S8d–i,† which were apparently enhanced as compared to the pre-annealed counterparts. Among them, CuSn–10C demonstrates the highest selectivity and geometric current for formate production by the CO_2RR, with a current density of 18.9 mA cm^{-2} at −1.0 V (Fig. S8g†). To evaluate the intrinsic activity of these CuSn intermetallic catalysts, the current density was normalized to the electrochemical surface area (ECSA) (Fig. S9†).[33–35] One can see that CuSn–10C exhibits a higher total current density for the CO_2RR (Fig. S10c†) and partial current density of HCOOH than CuSn–5C and CuSn–15C (Fig. 3d). As shown in Fig. 3e, the FE and current density for formate production coincide with the weight ratio of Cu_3Sn to Cu_6Sn_5 among the three samples, suggesting that the enhanced activity and selectivity towards formate production is most likely due to the formation of intermetallic Cu_3Sn/Cu_6Sn_5 heterostructures (Fig. 3c and S10a and b†), since the ECSAs of these CuSn alloys remained virtually invariant before and after thermal annealing.

The weight percentages of each of the components were calculated by the *K*-value method.[36]

To further demonstrate the significance of the Cu_3Sn/Cu_6Sn_5 heterostructure in CO_2RR activity and formate production, pure-phase Cu_3Sn and Cu_6Sn_5 (Fig. S11 and S12†) were prepared and their CO_2RR activity was analyzed and compared. Electrochemical measurements (Fig. S13 and S14a†) show that the CO_2RR on Cu_6Sn_5 and Cu_3Sn primarily produced H_2, with FEs of 75.3% and 57.5% at −1.0 V. In addition, both Cu_3Sn and Cu_6Sn_5 exhibited a higher activity towards H_2 and CO production than CuSn–10C (Fig. S14b–d†), suggesting that the formation of Cu_3Sn/Cu_6Sn_5 heterostructures might suppress both the H_2 evolution and CO production and promote the production of HCOOH.

The kinetic performance of the CO_2RR to produce formate was then evaluated by Tafel analysis of the partial currents for formate production (Fig. S15a–c†). Note that in the CO_2RR, a Tafel slope of 118 mV dec^{-1} typically suggests that the initial transfer of one electron to adsorbed CO_2 to form the CO_2^{*-} intermediate is the rate-determining step (RDS), while a Tafel

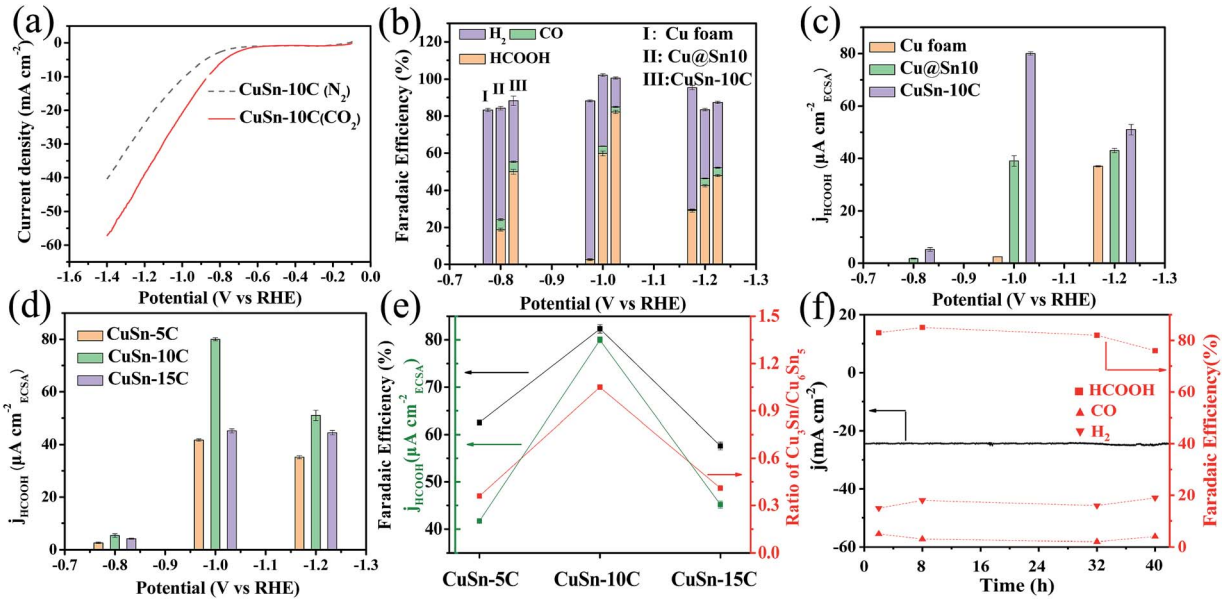

Fig. 3 (a) LSV curves of CuSn–10C in N_2- and CO_2-saturated 0.1 M $NaHCO_3$ electrolyte at a scan rate of 10 mV s^{-1}. (b) FE of various CO_2RR products on Cu foam, Cu@Sn10 and CuSn–10C. Partial current density of HCOOH normalized to the ECSA on (c) Cu foam, Cu@Sn10, and CuSn–10C, and (d) CuSn–5C, CuSn–10C, and CuSn–15C. The variation of FE, partial current density ((e), left axis) and mass ratio of Cu_3Sn to Cu_6Sn_5 on the heterostructured CuSn intermetallics. Stability test of CuSn–10C at −1.0 V *vs.* RHE for the CO_2RR (f).

slope of 59 mV dec^{-1} suggests that the protonation of CO_2^{*-} is the RDS.[37,38] The measured Tafel slopes for CuSn–5C (134 mV dec^{-1}), CuSn–10C (121 mV dec^{-1}) and CuSn–15C (129 mV dec^{-1}) suggest that the RDS on the three samples is the first electron-reduction of adsorbed CO_2. Furthermore, Fig. S15d† shows the Nyquist plots and the corresponding equivalent circuit of the three catalysts, which revealed that CuSn–10C displayed a lower interfacial charge-transfer resistance (R_{ct}) than CuSn–5C and CuSn–15C. To verify the binding affinity of CO_2^{*-} on the three alloys, adsorption of OH^- as a surrogate for CO_2^{*-} was conducted by oxidative LSV scans in a N_2-bubbled 0.1 M NaOH electrolyte.[39,40] The results (Fig. S16†) show that the potential for surface OH^- adsorption on CuSn–10C is the most negative, indicating a stronger adsorption affinity of the OH^- surrogate ion (CO_2^{*-}) on CuSn–10C, in good agreement with the maximal CO_2RR performance among all the catalysts (Fig. 3). The stability of the CuSn–10C catalyst was then tested. From Fig. 3f, the current density remains almost invariant after continuous operation for 42 h. In addition, no apparent change was observed in the LSV (Fig. S17a†), XRD (Fig. S17b†) and SEM (Fig. S18†) results, signifying high stability of the CuSn–10C catalyst for the CO_2RR. The final decrease in faradaic efficiency of formate may be caused by the destruction of the hetero-junction of the catalyst (Fig. S19†). Notably, in comparison to leading formate-selective electrocatalysts reported in recent literature, the CuSn–10C catalyst is highly comparable, in terms of overpotential, formate partial current density, and FE, as illustrated in Fig. S20 and Table S1.†

Due to the limited solubility of CO_2 in aqueous solution, it is very challenging to achieve a current density more than 100 mA cm^{-2} in an H-type cell. Moreover, alkaline electrolyte cannot be used in an H-type cell since CO_2 can react with an alkaline solution. Thus, the CuSn intermetallic catalysts were further tested in a flow cell with 1 M KOH electrolyte (Fig. 4a–c). A total current density of 210 mA cm^{-2} at −0.108 V (Fig. S21†) and a current density of 148 mA cm^{-2} for formate production with an FE of 87% were achieved at an applied potential of −0.98 V *versus* RHE (Fig. 4d). The electrochemical performances of CuSn–5C and CuSn–15C were also tested and the results, which are shown in Fig. S22,† were inferior to those of CuSn–10C.

DFT calculations were further performed to unravel the correlation between the CO_2RR activity and catalyst structure. The structural characterization of the CuSn catalysts has shown the formation of heterostructured intermetallic Cu_3Sn and Cu_6Sn_5 and the thickness of this layer was estimated to be approximately 200 nm on the CuSn–10C.[41,42] Therefore, DFT calculations were conducted on the metallic state Cu_3Sn, Cu_6Sn_5 and heterostructured Cu_3Sn/Cu_6Sn_5 without the interaction of the Cu substrate.[43] The computational analysis of the CO_2RR is focused on two major pathways, CO and $HCOO^-$ production with two-electron and two-proton transfer,[44–46] which is mainly determined by the adsorption energy of HCOO* and *COOH intermediates on the electrode surface.[41,45,47,48] As illustrated below, steps 1 and 4 are generally assumed to be the RDS of each pathway:[49]

Formic acid pathway[44,50]

$$CO_2(g) + e^- + H^+ + * \rightarrow HCOO* \quad (1)$$

$$HCOO* + e^- + H^+ \rightarrow HCOOH* \quad (2)$$

$$HCOOH* \rightarrow HCOOH(aq) + * \quad (3)$$

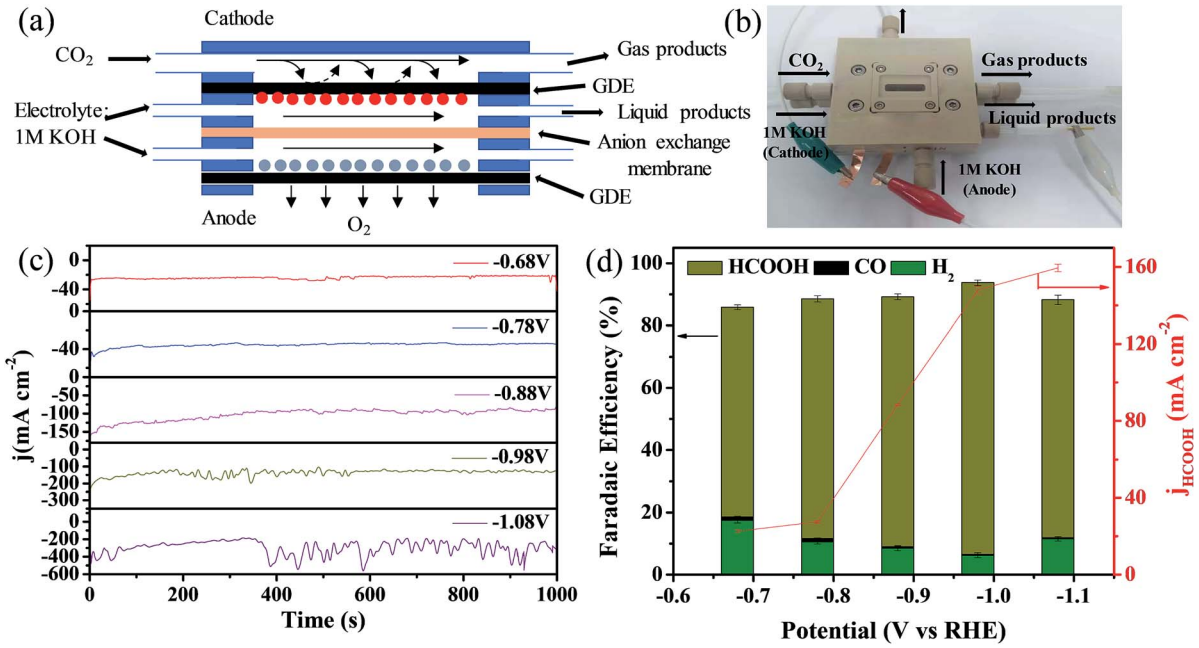

Fig. 4 (a) Schematic illustration and (b) physical image of a flow cell using 1 M KOH electrolyte. (c) Chronoamperometric curves at various potentials and (d) FE and partial current density of HCOOH for the CO_2RR on CuSn–10C.

Carbon monoxide pathway[26,51,52]

$$CO_2(g) + e^- + H^+ + * \rightarrow *COOH \quad (4)$$

$$*COOH + e^- + H^+ \rightarrow *CO + H_2O(l) \quad (5)$$

$$*CO \rightarrow CO(g) + * \quad (6)$$

The energetics of the key reaction intermediates involved in the CO and formate pathways on Cu_3Sn, Cu_6Sn_5 and heterostructured Cu_3Sn/Cu_6Sn_5 are shown in Fig. 5a, S23–S26† and Table 2. The adsorption energies of HCOO* are much more negative than those of COOH* on Cu_3Sn, Cu_6Sn_5 and Cu_3Sn/Cu_6Sn_5, suggesting that the formation of formate is more highly preferred than the formation of CO on these catalysts. Furthermore, the energetics difference between HCOO* and COOH* (1.76 eV) on heterostructured Cu_3Sn/Cu_6Sn_5 is enhanced by 0.7 eV, as compared to that on pure-phase Cu_3Sn and Cu_6Sn_5, suggesting that the selectivity of formate is further favoured by the formation of the heterostructured intermetallics. In contrast to that of Cu_3Sn, Cu_6Sn_5 and Cu_3Sn/Cu_6Sn_5, the potential limiting step for the formate production on Cu and Sn is believed to be the formation of COOH*,[53] which is also the intermediate of CO production. Since the desorption of CO from Cu is

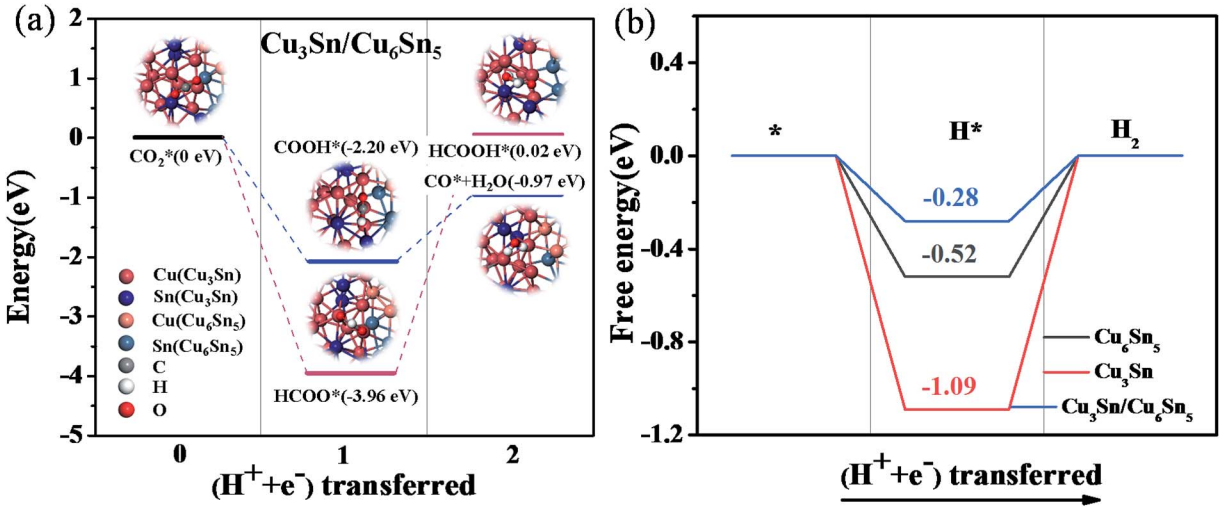

Fig. 5 (a) Calculated energy diagrams of key CO_2RR intermediates for CO (blue) and HCOOH (brown) production on the heterostructured Cu_3Sn/Cu_6Sn_5 surface. (b) Calculated free-energy diagram of the HER on Cu_6Sn_5, Cu_3Sn and heterostructured Cu_3Sn/Cu_6Sn_5.

Table 2 Summary of DFT calculation of the energetics characteristics of CO_2RR intermediates

	Intermediates	$Cu_3Sn(111)$	$Cu_6Sn_5(111)$	Cu_3Sn/Cu_6Sn_5
Binding energy (eV)	COOH*	−2.90	−1.87	−2.20
	HCOO*	−4.05	−3.00	−3.96
ΔG (eV)	H*	−1.09	−0.52	−0.28
ΔE (eV)	|EHCOO*–ECOOH*|	1.15	1.13	1.76

endothermic, hydrocarbons were produced on Cu catalysts due to C–C coupling of adsorbed CO. However, due to the low Gibbs free energy of hydrogen atoms on Cu, the HER is very competitive with the CO_2RR on the Cu surface and low FE of formate production was observed, in agreement with our results.[53]

The Gibbs free energy of the HER on intermetallic CuSn is shown in Fig. 5b and S27.† Too strong adsorption of hydrogen may block the active site and reduce the catalytic performance for the CO_2RR, as observed on Cu_3Sn (−1.09 eV) and Cu_6Sn_5 (−0.52 eV), making them poor catalysts for formic acid production. However, heterostructured Cu_3Sn/Cu_6Sn_5 (−0.28 eV) shows moderate adsorption of hydrogen and high formate production activity, since the CO_2RR consumes adsorbed H for formate production and the moderate adsorption of H on the catalyst surface favors the CO_2RR.[54–57] In summary, results from the DFT calculations suggest that the heterostructured Cu_3Sn/Cu_6Sn_5 is more conducive to the CO_2RR and selective production of formic acid due to moderate adsorption of hydrogen, consistent with experimental results.

Conclusions

In summary, an electrodeposition–calcination process was developed to prepare Cu_3Sn/Cu_6Sn_5 intermetallic heterostructures which exhibited a FE of 82% for the CO_2RR to produce formate at −1.0 V *vs.* RHE and a current density of 18.9 mA cm^{-2} for up to 42 h in 0.1 M $NaHCO_3$ electrolyte. By using a gas diffusion electrode and 1 M KOH electrolyte, a current density of 148 mA cm^{-2} and an FE of 87% toward formate production were achieved. A combination of experiments and theoretical calculations revealed that the high catalytic activity was primarily due to the interface between the Cu_6Sn_5 and Cu_3Sn intermetallics, where the adsorption of the HCOO* intermediate was stronger than that of COOH* and the free energy of adsorbed hydrogen was upshifted, leading to the suppression of hydrogen evolution and selective production of formate. Results from the present study demonstrate the feasibility of employing low-cost, non-noble metals to produce bimetallic electrocatalysts for the CO_2RR with high efficiency, stability, and selectivity.

Conflicts of interest

The authors declare no competing financial interest.

Acknowledgements

This work was supported by the National Key R&D Program of China (No. 2018YFB1502600), the National Natural Science Foundation of China (No. 21773224), the Fundamental Research Funds for the Central Universities (SCUT Grant No. 2019ZD22) and the Guangdong Innovative and Entrepreneurial Research Team Program (No. 2016ZT06N569).

References

1 D. R. Kauffman, J. Thakkar, R. Siva, C. Matranga, P. R. Ohodnicki, C. Zeng and R. Jin, *ACS Appl. Mater. Interfaces*, 2015, **7**, 15626–15632.
2 J. Qiao, Y. Liu, F. Hong and J. Zhang, *Chem. Soc. Rev.*, 2014, **43**, 631–675.
3 N. S. Spinner, J. A. Vega and W. E. Mustain, *Catal. Sci. Technol.*, 2012, **2**, 19–28.
4 S. Q. Zhu, Q. Wang, X. P. Qin, M. Gu, R. Tao, B. P. Lee, L. L. Zhang, Y. Z. Yao, T. H. Li and M. H. Shao, *Adv. Energy Mater.*, 2018, **8**, 1802238.
5 S. Q. Zhu, B. Jiang, W. B. Cai and M. H. Shao, *J. Am. Chem. Soc.*, 2017, **139**, 15664–15667.
6 S. Q. Zhu, T. H. Li, W. B. Cai and M. H. Shao, *ACS Energy Lett.*, 2019, **4**, 682–689.
7 Z. Zhang, C. Liu, J. T. Brosnahan, H. Zhou, W. Xu and S. Zhang, *J. Mater. Chem. A*, 2019, **7**, 23775–23780.
8 Y. Ma, Z. J. Wang, C. Yang, A. X. Guan, L. M. Shang, A. M. Al-Enizi, L. J. Zhang and G. F. Zheng, *J. Mater. Chem. A*, 2018, **6**, 20121–20127.
9 P. Yang, Z.-J. Zhao, X. Chang, R. Mu, S. Zha, G. Zhang and J. Gong, *Angew. Chem.*, 2018, **130**, 7850–7854.
10 S. Zhu, B. Jiang, W.-B. Cai and M. Shao, *J. Am. Chem. Soc.*, 2017, **139**, 15664–15667.
11 Y. Hori, A. Murata and R. Takahashi, *J. Chem. Soc., Faraday Trans. 1*, 1989, **85**, 2309–2326.
12 K. J. P. Schouten, Y. Kwon, C. J. M. van der Ham, Z. Qin and M. T. M. Koper, *Chem. Sci.*, 2011, **2**, 1902–1909.
13 C. Zhao and J. Wang, *Chem. Eng. J.*, 2016, **293**, 161–170.
14 H. Won Da, H. Choi Chang, J. Chung, W. Chung Min, E. H. Kim and I. Woo Seong, *ChemSusChem*, 2015, **8**, 3092–3098.
15 S. Nitopi, E. Bertheussen, S. B. Scott, X. Liu, A. K. Engstfeld, S. Horch, B. Seger, I. E. L. Stephens, K. Chan, C. Hahn, J. K. Nørskov, T. F. Jaramillo and I. Chorkendorff, *Chem. Rev.*, 2019, **119**, 7610–7672.
16 G. Wen, D. U. Lee, B. Ren, F. M. Hassan, G. Jiang, Z. P. Cano, J. Gostick, E. Croiset, Z. Bai, L. Yang and Z. Chen, *Adv. Energy Mater.*, 2018, **8**, 1802427.
17 D. Ren, B. S.-H. Ang and B. S. Yeo, *ACS Catal.*, 2016, **6**, 8239–8247.
18 Z. Gu, H. Shen, L. Shang, X. Lv, L. Qian and G. Zheng, *Small Methods*, 2018, **3**, 1800449.

19 S. Sarfraz, A. T. Garcia-Esparza, A. Jedidi, L. Cavallo and K. Takanabe, *ACS Catal.*, 2016, **6**, 2842–2851.
20 X. Bai, W. Chen, C. Zhao, S. Li, Y. Song, R. Ge, W. Wei and Y. Sun, *Angew. Chem.*, 2017, **129**, 12387–12391.
21 Y. Wang, P. Han, X. Lv, L. Zhang and G. Zheng, *Joule*, 2018, **2**, 2551–2582.
22 D. Zhu, J. Liu, Y. Zhao, Y. Zheng and S.-Z. Qiao, *Small*, 2019, **15**, 1805511.
23 J. Wang, F. Zhang, X. Kang and S. Chen, *Curr. Opin. Electrochem.*, 2019, **13**, 40–46.
24 K. Wang, X. She, S. Chen, H. Liu, D. Li, Y. Wang, H. Zhang, D. Yang and X. Yao, *J. Mater. Chem. A*, 2018, **6**, 5560–5565.
25 C. Zhu, A.-L. Wang, W. Xiao, D. Chao, X. Zhang, N. H. Tiep, S. Chen, J. Kang, X. Wang, J. Ding, J. Wang, H. Zhang and H. J. Fan, *Adv. Mater.*, 2018, **30**, 1705516.
26 S. Sen, D. Liu and G. T. R. Palmore, *ACS Catal.*, 2014, **4**, 3091–3095.
27 J. Cheng, M. Zhang, J. Liu, J. Zhou and K. Cen, *J. Mater. Chem. A*, 2015, **3**, 12947–12957.
28 M. F. Baruch, J. E. Pander, J. L. White and A. B. Bocarsly, *ACS Catal.*, 2015, **5**, 3148–3156.
29 Y. Chen and M. W. Kanan, *J. Am. Chem. Soc.*, 2012, **134**, 1986–1989.
30 A. Dutta, A. Kuzume, M. Rahaman, S. Vesztergom and P. Broekmann, *ACS Catal.*, 2015, **5**, 7498–7502.
31 S. Lee, J. D. Ocon, Y.-i. Son and J. Lee, *J. Phys. Chem. C*, 2015, **119**, 4884–4890.
32 Y. Zhang, L. Li, Q. Li, J. Fan, J. Zheng and G. Li, *Chem.–Eur. J.*, 2016, **22**, 14196–14204.
33 C. W. Li, J. Ciston and M. W. Kanan, *Nature*, 2014, **508**, 504–507.
34 X. Zheng, P. De Luna, F. P. García de Arquer, B. Zhang, N. Becknell, M. B. Ross, Y. Li, M. N. Banis, Y. Li, M. Liu, O. Voznyy, C. T. Dinh, T. Zhuang, P. Stadler, Y. Cui, X. Du, P. Yang and E. H. Sargent, *Joule*, 2017, **1**, 794–805.
35 X. Zheng, Y. Ji, J. Tang, J. Wang, B. Liu, H.-G. Steinrück, K. Lim, Y. Li, M. F. Toney, K. Chan and Y. Cui, *Nat. Catal.*, 2019, **2**, 55–61.
36 L. Alexander and H. P. Klug, *Anal. Chem.*, 1948, **20**, 886–889.
37 X. Cui, Z. Pan, L. Zhang, H. Peng and G. Zheng, *Adv. Energy Mater.*, 2017, **7**, 1701456.
38 A. Zhang, R. He, H. Li, Y. Chen, T. Kong, K. Li, H. Ju, J. Zhu, W. Zhu and J. Zeng, *Angew. Chem., Int. Ed.*, 2018, **57**, 10954–10958.
39 F. Lei, W. Liu, Y. Sun, J. Xu, K. Liu, L. Liang, T. Yao, B. Pan, S. Wei and Y. Xie, *Nat. Commun.*, 2016, **7**, 12697.
40 X. Wang, Z. Chen, X. Zhao, T. Yao, W. Chen, R. You, C. Zhao, G. Wu, J. Wang, W. Huang, J. Yang, X. Hong, S. Wei, Y. Wu and Y. Li, *Angew. Chem., Int. Ed.*, 2018, **57**, 1944–1948.
41 Q. Li, J. Fu, W. Zhu, Z. Chen, B. Shen, L. Wu, Z. Xi, T. Wang, G. Lu, J.-j. Zhu and S. Sun, *J. Am. Chem. Soc.*, 2017, **139**, 4290–4293.
42 R. Zhang, W. Lv, G. Li and L. Lei, *Mater. Lett.*, 2015, **141**, 63–66.
43 C. W. Li and M. W. Kanan, *J. Am. Chem. Soc.*, 2012, **134**, 7231–7234.
44 A. Klinkova, P. De Luna, C.-T. Dinh, O. Voznyy, E. M. Larin, E. Kumacheva and E. H. Sargent, *ACS Catal.*, 2016, **6**, 8115–8120.
45 J. S. Yoo, R. Christensen, T. Vegge, J. K. Nørskov and F. Studt, *ChemSusChem*, 2015, **9**, 358–363.
46 M. Dunwell, Y. Yan and B. Xu, *ACS Catal.*, 2017, **7**, 5410–5419.
47 J. Wu, R. M. Yadav, M. Liu, P. P. Sharma, C. S. Tiwary, L. Ma, X. Zou, X.-D. Zhou, B. I. Yakobson, J. Lou and P. M. Ajayan, *ACS Nano*, 2015, **9**, 5364–5371.
48 V.-A. Glezakou, L. X. Dang and B. P. McGrail, *J. Phys. Chem. C*, 2009, **113**, 3691–3696.
49 A. Wuttig, M. Yaguchi, K. Motobayashi, M. Osawa and Y. Surendranath, *Proc. Natl. Acad. Sci. U. S. A.*, 2016, **113**, E4585.
50 S. Zhang, P. Kang and T. J. Meyer, *J. Am. Chem. Soc.*, 2014, **136**, 1734–1737.
51 H. Huang, H. Jia, Z. Liu, P. Gao, J. Zhao, Z. Luo, J. Yang and J. Zeng, *Angew. Chem., Int. Ed.*, 2017, **56**, 3594–3598.
52 K. Jiang, S. Siahrostami, A. J. Akey, Y. Li, Z. Lu, J. Lattimer, Y. Hu, C. Stokes, M. Gangishetty, G. Chen, Y. Zhou, W. Hill, W.-B. Cai, D. Bell, K. Chan, J. K. Nørskov, Y. Cui and H. Wang, *Chem*, 2017, **3**, 950–960.
53 X. Zheng, Y. Ji, J. Tang, J. Wang, B. Liu, H.-G. Steinrück, K. Lim, Y. Li, M. F. Toney, K. Chan and Y. Cui, *Nat. Catal.*, 2019, **2**, 55–61.
54 W. Ma, S. Xie, X.-G. Zhang, F. Sun, J. Kang, Z. Jiang, Q. Zhang, D.-Y. Wu and Y. Wang, *Nat. Commun.*, 2019, **10**, 892.
55 K. Ohkawa, K. Hashimoto, A. Fujishima, Y. Noguchi and S. Nakayama, *J. Electroanal. Chem.*, 1993, **345**, 445–456.
56 K. Ohkawa, Y. Noguchi, S. Nakayama, K. Hashimoto and A. Fujishima, *J. Electroanal. Chem.*, 1993, **348**, 459–464.
57 K. Ohkawa, Y. Noguchi, S. Nakayama, K. Hashimoto and A. Fujishima, *J. Electroanal. Chem.*, 1994, **367**, 165–173.